Formability Assessment of Prestrained Automotive Grade Steel Sheets Using Stress Based and Polar Effective Plastic Strain-Forming Limit Diagram

S. Basak
Department of Mechanical Engineering,
Indian Institute of Technology Kharagpur,
West Bengal 721302, India
e-mail: shamik.iit@gmail.com

S. K. Panda
Assistant Professor
Department of Mechanical Engineering,
Indian Institute of Technology Kharagpur,
West Bengal 721302, India
e-mail: sushanta.panda@mech.iitkgp.ernet.in

Y. N. Zhou
Department of Mechanical and
Mechatronics Engineering,
University of Waterloo,
200 University Avenue West,
Waterloo, ON N2L 3G1, Canada
e-mail: nzhou@uwaterloo.ca

Accurate prediction of the formability in multistage forming process is very challenging due to the dynamic shift of limiting strain during the different stages depending on the tooling geometry and selection of the process parameters. Hence, in the present work, a mathematical framework is proposed for the estimation of stress based and polar effective plastic strain-forming limit diagram (σ- and PEPS-FLD) using the Barlat-89 anisotropic plasticity theory in conjunction with three different hardening laws such as Hollomon, Swift, and modified Voce equation. Two-stage stretch forming setup had been designed and fabricated to first prestrain in an in-plane stretch forming setup, and, subsequently, limiting dome height (LDH) testing was carried out on the prestrained blanks in the second stage to evaluate the formability. The finite element (FE) analysis of these two-stage forming process was carried out in LS-DYNA for automotive grade dual-phase (DP) and interstitial-free (IF) steels, and the σ-FLD and PEPS-FLD were used as damage model to predict failure. The predicted forming behaviors, such as LDH, thinning development, and the load progression, were validated with the experimental results. It was found that the LDH in the second stage decreased with increase in the prestrain amount, and both the σ-FLD and PEPS-FLD could be able to predict the formability considering the deformation histories in the present multistage forming process with complex strain path. [DOI: 10.1115/1.4030786]

Keywords: stress based-forming limit diagram, polar effective plastic strain-forming limit diagram, finite element analysis, multistage forming process, limiting dome height

1 Introduction

In sheet metal forming industries, a precise prediction of the formability is extremely important to manufacture various defect-free three-dimensional components at a high production rate. Hence, sheet metal forming researchers evaluate formability using various laboratory scale simulative tests without wasting much materials, and some of these popular tests are LDH, limiting drawing ratio, hole expansion ratio, bendability, and FLD. Out of these methods, the conventional FLD or ε-FLD is extensively used in the press shop floor as diagnostic tool to avoid early thinning/failure by selecting suitable tool design, process parameters, and blank material. The research on ε-FLD was started by Keeler and Backofen [1], and they diagrammed the limiting maximum principal strain (ε_1) against minimum principal strain (ε_2) for biaxially stretched specimens. Subsequently, Goodwin [2] plotted the ε_1 and ε_2 data on the same curve for tension–compression domain $(\varepsilon_1 > 0;\ \varepsilon_2 < 0)$. Hence, the Keeler and Goodwin curve which is popularly known as ε-FLD covers all the limiting strains those are possible under different loading paths, e.g., uniaxial, plane strain, biaxial, and equibiaxial, and it is determined by the classical circular grid analysis. Many researchers inferred that ε-FLD strongly depended on several factors, among which most predominant factors were strain hardening exponent, strain rate sensitivity index, Linkford anisotropy coefficient, and thickness of the sheet metal [3,4]. The main restriction of the use of ε-FLD is the dynamic shift during the multistage forming process due to the complex strain path. The dynamic nature of ε-FLD with different strain path was confirmed with a series of experiments on different materials by many early researchers, such as Matsuoka and Sudo [5], Muschenborn and Sonne [6], and Laukonis and Ghosh [7]. Graf and Hosford [8] supported this fact through extensive laboratory studies on Al 2008 T4 material. They reported that forming limit decreased with biaxial prestrain, and simultaneously shifted toward the tension–tension side. Similarly, the limiting strain increased both with uniaxial and plane strain prestrain for the same material by shifting toward the left and upside, respectively. To reduce or remove this dependency on strain path, an alternative damage model was proposed by Kleemola and Pelkkikangas [9], Arrieux et al. [10], and Stoughton [11,12], which was known as σ-FLD. They constructed σ-FLD by plotting the calculated major and minor principal stresses at necking. Yoshida et al. [13] and Zeng et al. [14] concluded that formability prediction of sheet metals should be based on stress state rather than strain state so as to avoid the deformation path dependency in the multistage forming processes. In spite of the successful applications, several researchers showed concern about the reduction in slope of true stress–true strain diagram, and hence, the robustness of σ-FLD. They indicated that σ-FLD is not much sensitive at large strains near to the necking limit due to the saturation of true stress–true strain curve. To encounter this problem, Stoughton and Yoon [15] proposed PEPS-FLD, which is a two-dimensional Cartesian

Contributed by the Materials Division of ASME for publication in the JOURNAL OF ENGINEERING MATERIALS AND TECHNOLOGY. Manuscript received March 29, 2015; final manuscript received May 21, 2015; published online June 26, 2015. Assoc. Editor: Tetsuya Ohashi.

coordinate mapping of limiting strain in effective plastic strain space. They concluded that the PEPS-FLD was less sensitive to change of strain path, and hence, it could be one effective tool to predict formability in a complex forming process.

Recently, the automotive industries are eager to apply advanced high-strength grade DP steels to fabricate light-weight components by thinning down the gauge. These steels are also characterized to have improved strength, crashworthiness, and fatigue resistance compared to conventional precipitation alloyed high-strength steels. Ti and Nb microalloyed IF steels have been also developed recently for manufacturing complex shaped structural and exterior automotive parts due to its excellent cold formability. In practice, the complex automotive stampings may undergo several sheet forming passes using different die and punch shapes. During these different passes, the deformation path in terms of strain ratio may not be constant, but it changes depending on choice of die design and process parameters. Hence, an accurate prediction of the forming limit during the changing strain path is very challenging for both DP and IF steels for automotive body applications.

In this paper, a comparative study is made for prediction of formability on DP600 (a commercial grade DP steel) and IF steel sheets by σ-FLD and PEPS-FLD during the multistage forming process. To establish a complex strain path, which is a combination of two linear stain paths, two-stage stretch forming setup was designed. The prestraining in the blank was induced by an in-plane stretch forming setup in the first stage, and the out-of-plane stretch forming was carried out on the prestrained blank to find the formability in terms of LDH in the second stage. Mathematical framework was proposed to estimate the σ-FLD and PEPS-FLD from the experimental ε-FLD using Barlat-89 anisotropic material model incorporating Hollomon, Swift, and modified Voce hardening laws. The FE analysis of the two-stage stretch forming processes was carried out in LS-DYNA. Both of the theoretical models, σ-FLD and PEPS-FLD, were implemented as a damage model to predict the forming behavior of prestrained materials, and the outcomes were validated with the experimental results.

2 Analytical Approach for σ- and PEPS-FLD

In order to get the complete shape of ε-FLD, many researchers proposed different tests for characterizing the limiting strains in the different regions of the curve. Among them, few important tests, mostly referred by researchers, are: uniaxial tensile, hydraulic bulging [16], Hecker's out-of-plane stretching [17], Marciniak's in-plane stretching [18], Nakazima's cupping [19], and Hasek's test [20]. However, the stress state cannot be determined directly from these tests during forming. The following three correlations are required to transfer the limiting strain to stress state: (a) yield function, $f(\sigma_1, \sigma_2, \sigma_3, \bar{\sigma}) = 0$, where σ_1, σ_2, and σ_3 are the components of principal stresses and $\bar{\sigma}$ is the effective stress obtained from tensile test; (b) associated flow rule to relate the components of stress and strain; and (c) hardening rule for describing the evolution of effective stress during the forming process. In this work, the Barlat-89 yield criterion [21] with three hardening laws (e.g., Hollomon, Swift, and modified Voce hardening law) is used to estimate σ-FLD from ε-FLD.

2.1 Theoretical Background of Constitutive Model. The Barlat-89 yield function incorporating the normal and planar anisotropy during the plane stress deformation was selected for the modeling of the deformable blank as described by the following equation:

$$\bar{\sigma}(\sigma_{ij}) = \left[1/2 \times \left(a|k_1 + k_2|^M + a|k_1 - k_2|^M + c|2k_2|^M\right)\right]^{1/M} \tag{1}$$

where $a, c,$ and h are material constants related to Lankford anisotropy parameters r_0 and r_{90} as shown in the following equation:

$$a = 2 - c = 2 - 2\sqrt{\frac{r_0}{1+r_0} \times \frac{r_{90}}{1+r_{90}}} \text{ and}$$
$$h = \sqrt{\frac{r_0}{1+r_0} \times \frac{1+r_{90}}{r_{90}}} \tag{2}$$

For polycrystalline steel sheet, the value of the nonquadratic Barlat exponent, M, is chosen to be six. As in the present sheet forming experiments, the anisotropic thin-rolled sheets were considered, the shear stress was assumed to be neglected so as to reduce the complexity in the analytical formulation. When stress tensor (σ_{ij}) coincides with the principal anisotropic axis of the sheet metal, the invariants of stress tensor, k_1 and k_2, are defined as shown in the following equation:

$$k_1 + k_2 = \sigma_1 \quad \text{and} \quad k_1 - k_2 = h \cdot \sigma_2 \tag{3}$$

Substituting Eq. (3), Eq. (1) reduces to

$$\bar{\sigma}(\sigma_{ij}) = \left[1/2 \times \left(a|\sigma_1|^M + a|h\sigma_2|^M + c|\sigma_1 - h\sigma_2|^M\right)\right]^{1/M} \tag{4}$$

Applying flow rule, $d\varepsilon_{ij} = d\lambda\left[\left(\partial\bar{\sigma}(\sigma_{ij})\right)/\partial\sigma_{ij}\right]$ (where $d\lambda$ is a positive scalar that depends on the stress state) in Eq. (4), and upon simplification the equation can be written in the form of stress ratio ξ, defined as the ratio of effect stress ($\bar{\sigma}$) to major stress (σ_1) as

$$\xi = \left[1/2 \times \left(a + a|h\alpha|^M + c|1 - h\alpha|^M\right)\right]^{1/M}, \quad \text{where } \alpha = \frac{\sigma_2}{\sigma_1} \tag{5}$$

Again, the strain ratio $\rho = d\varepsilon_2/d\varepsilon_1$ can be written in the form of $\alpha(\rho)$ as

$$\rho = \frac{a|h\alpha|^{M-1} - ch|1 - h\alpha|^{M-1}}{a + c|1 - h\alpha|^{M-1}} \tag{6}$$

From the definition of plastic work ($\bar{\sigma} \cdot d\bar{\varepsilon} = \sigma_1 \cdot d\varepsilon_1 + \sigma_2 \cdot d\varepsilon_2 + \sigma_3 \cdot d\varepsilon_3$) and further imposing the plane stress condition ($\sigma_3 = 0$), the effective strain can be expressed in the form

$$\bar{\varepsilon} = \frac{\varepsilon_1}{\xi}(1 + \rho\alpha) \tag{7}$$

In order to establish the hardening relationship between true effective stress and true effective strain, three functions were chosen, and these are Hollomon, Swift, and modified Voce hardening laws, as indicated in Eqs. (8)–(10), respectively,

$$\bar{\sigma} = K \cdot \bar{\varepsilon}^n \tag{8}$$

$$\bar{\sigma} = K \cdot (\varepsilon_0 + \bar{\varepsilon})^n \tag{9}$$

$$\bar{\sigma} = A - B_0 \cdot e^{(-C \cdot \bar{\varepsilon})} + B_1 \cdot \bar{\varepsilon} \tag{10}$$

where $\bar{\sigma}$ and $\bar{\varepsilon}$ are, respectively, the effective stress and plastic strain. K (strength coefficient), n (strain hardening exponent), and ε_0, A, B_0, B_1, and C are the material constants. All these constants can be calculated by fitting the experimentally determined true stress–true strain curve in MATLAB. B_1 is approximately identified in this work as half of yield strength value for each of the investigated steels.

2.2 Global Algorithm for Constructing σ-FLD and PEPS-FLD. The algorithm, as shown in Fig. 1, is proposed to compute the σ-FLD and PEPS-FLD from a given ε-FLD by considering the constitutive equation discussed in Sec. 2.1. However, the steps involved are again discussed as below, where the first two steps are common for estimating both σ-FLD and PEPS-FLD:

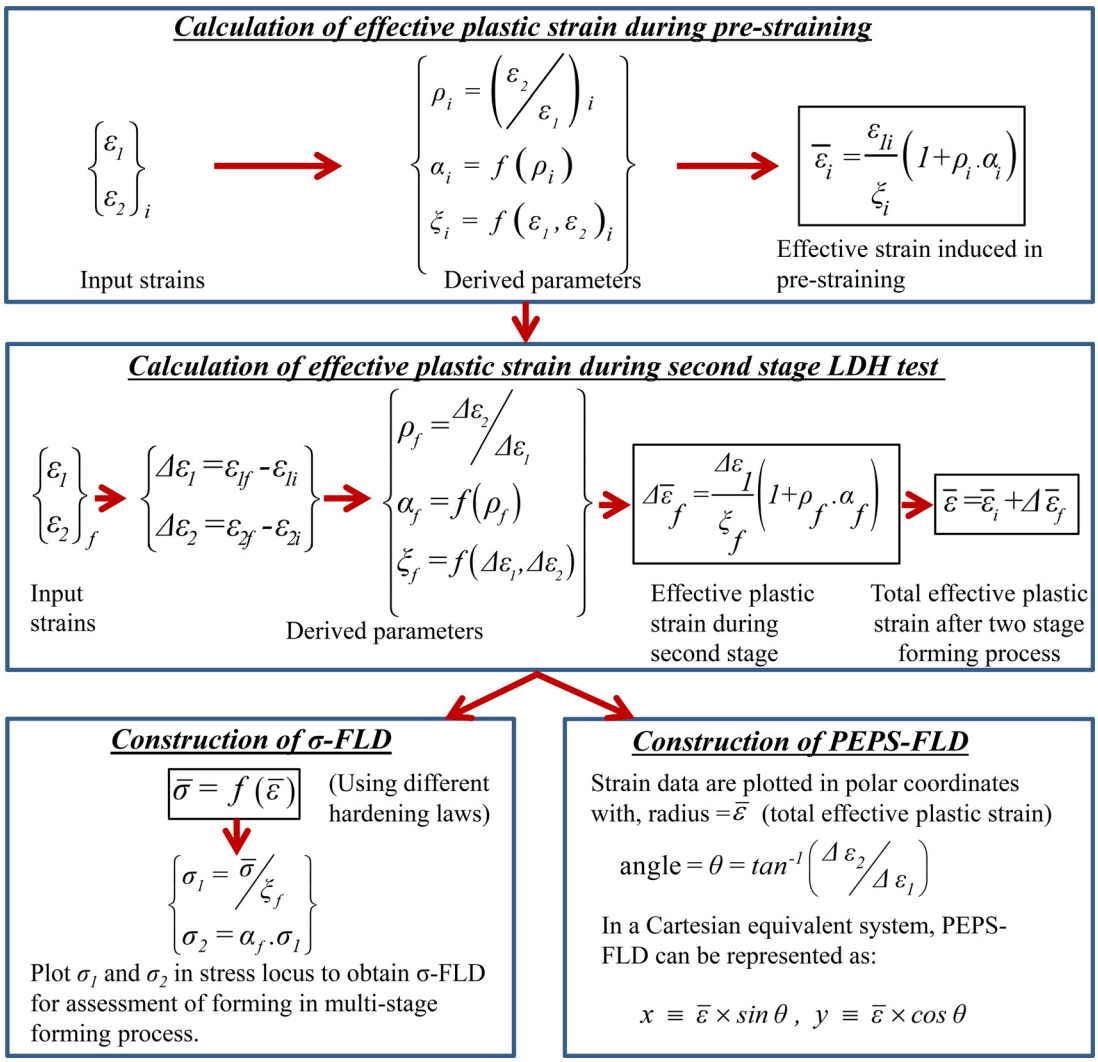

Fig. 1 Proposed mathematical framework for construction of σ-FLD and PEPS-FLD

Step 1: The principal strains $(\varepsilon_1,\varepsilon_2)_i$ were measured after the prestraining, and corresponding strain ratio $(\rho_i=(\varepsilon_2/\varepsilon_1)_i)$ had been calculated. The stress ratio, $\alpha_i(\rho_i)$, was calculated for each of the strain ratio, ρ_i, by using Eq. (6). Another derived parameter, ξ_i, was calculated using Eq. (5) for each value of the stress ratio, α_i. The final effective plastic strain $(\bar{\varepsilon}_i)$ in the prestraining stage was evaluated from the definition of plastic work (Eq. (7)).

Step 2: Final principal strains after second stage $(\varepsilon_1,\varepsilon_2)_f$ were again measured, and the corresponding plastic strain increment $(\Delta\varepsilon_1,\Delta\varepsilon_2)$ was estimated. The effective plastic strain increment $(\Delta\bar{\varepsilon}_f)$ was calculated from the principal plastic strain increments using the second stage derived parameters, ρ_f, ξ_f, and α_f as shown in the algorithm above. As true strains are additive in nature, hence, the total effective plastic strain $(\bar{\varepsilon})$ was calculated by adding the effective plastic strains of each steps.

Step 3 (*for σ-FLD*): Final effective stress $(\bar{\sigma})$ was obtained using different hardening laws (Eqs. (8)–(10)) from the knowledge of total effective strain $(\bar{\varepsilon})$. Finally, the major and minor stresses (σ_1 and σ_2) were calculated using the derived parameters ξ_f and α_f as discussed in the algorithm, and these values were plotted in stress locus to obtain σ-FLD.

Step 4 (*for PEPS-FLD*): It is a polar representation of the effective plastic strain with the direction defined by the arctangent of the current plastic strain increment ratio $(\Delta\varepsilon_2/\Delta\varepsilon_1)$. For better visualization, PEPS-FLD was plotted in Cartesian coordinate system in effective plastic strain space as shown in the algorithm.

This algorithm was implemented in MATLAB 8.1 on a Windows environment to estimate the σ-FLD and PEPS-FLD from the given ε-FLD of an anisotropic steel sheet.

2.3 Use of σ-FLD and PEPS-FLD as a Measure of Formability. In this particular work, the ε-FLDs of DP600 and IF of 1.2 mm sheet thickness were taken from the available literature [22,23]. For DP600, ε-FLD was plotted in Fig. 2(*a*) with three major strain paths, viz., equibiaxial strain path $(\rho = 1)$, plane strain path $(\rho = 0)$, and uniaxial strain path $(\rho = -0.5)$. It can be seen that the data point represents the strain paths, $\rho = 1$ and $\rho = -0.5$, were absent as the hydraulic bulging and uniaxial tests were not performed by the authors. The limiting strain is the minimum at the plane strain deformation path. Also, the forming limit of IF steel is lying above that of the DP600 steel. This is due to the higher *n*-value and *r*-value of IF compared to that of DP600. The strain data of the ε-FLD were converted to stress locus by calculating different derived constants like ξ, α, and ρ, as mentioned in Sec. 2.2, and the σ-FLD of both the material was plotted in Fig. 2(*b*). It can be seen from the figure that the Swift hardening law predicts a higher forming limit stresses compare to the other two cases. Also at the pure biaxial condition, the modified Voce law gives the lowest prediction of forming limit stress. The limiting stresses of DP600 steel are lying above those of IF steel, which is contradictory to their formability.

In order to judge the dynamic nature of ε-FLD, a reversal technique is adopted in this paper. A single curve in stress space

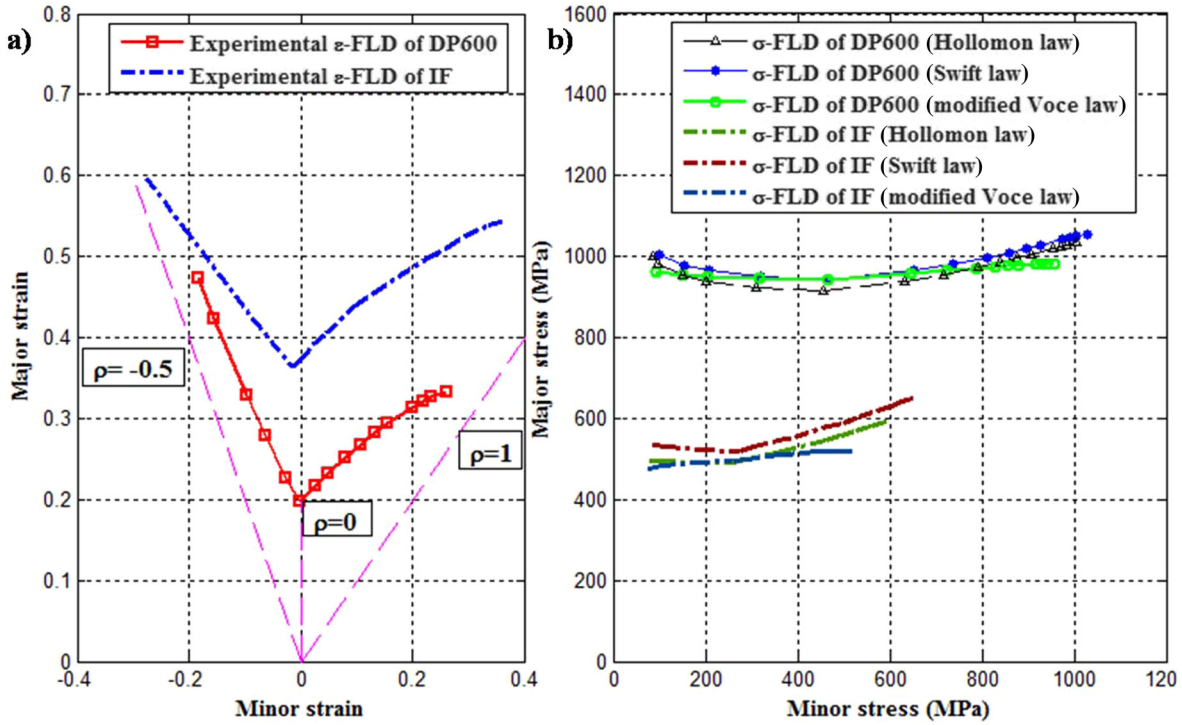

Fig. 2 Comparison of forming limit of DP600 and IF steels: (*a*) experimental ε-FLD [22,23] and (*b*) estimated σ-FLD using Barlat-89 yield criterion in conjunction with hardening laws

(σ-FLD predicted by Swift hardening law in Fig. 2(*b*)) was decoupled into strain space (ε-FLD) for 6.3% and 11.3% biaxial prestrain. To evaluate the decoupled FLD for a definite prestrain, the major (σ_1) and minor (σ_2) stress values were noted from the σ-FLD. From the stress ratio α_f, the other important parameters like ρ_f and ξ_f were calculated by using Eqs. (6) and (5), respectively. Using these parameters $(\sigma_1$ and $\xi_f)$, the effective stress $(\bar{\sigma})$ was evaluated, and the total effective strains $(\bar{\varepsilon})$ after forming in both the stages were obtained incorporating the hardening laws. From the knowledge of the amount of prestrain $(\varepsilon_{1i},\varepsilon_{2i})$, the effective strain $(\bar{\varepsilon}_i)$ during prestrain was calculated as shown in the algorithm (Fig. 1). The effective strain in the second stage $(\Delta\varepsilon_f)$ can be easily evaluated by the following equation:

$$\Delta\varepsilon_f = f\{\bar{\varepsilon}(\sigma_1,\sigma_2) - \bar{\varepsilon}_i(\varepsilon_{1i},\varepsilon_{2i})\} \tag{11}$$

From the plastic work Eq. (7), the increment in major strain $(\Delta\varepsilon_1)$ was computed, and consequently the increment in minor strain $(\Delta\varepsilon_2)$ was estimated from the ratio ρ_f. Finally, the major (ε_{1f}) and minor (ε_{2f}) strains of decoupled FLD were estimated by the following equation:

$$\varepsilon_{1f} = \varepsilon_{1i} + \Delta\varepsilon_1 \quad \text{and} \quad \varepsilon_{2f} = \varepsilon_{2i} + \Delta\varepsilon_2 \tag{12}$$

Major and minor strains of decoupled FLD for two different biaxial prestrain conditions 6.3% and 11.3% were plotted in strain locus as shown in Fig. 3(*a*). It can be seen that the forming limit of ε-FLDs for biaxial prestraining reduces, and similar results were reported by previous researchers [8] for aluminum alloy.

Furthermore to understand the capability of PEPS-FLD, all the theoretical decoupled ε-FLDs generated from a single σ-FLD were converted into effective plastic strain domain, as shown in Fig. 3(*b*). Interestingly, all the theoretical decoupled ε-FLDs are exactly merging into a single curve with as-received ε-FLD in polar coordinate strain space of PEPS-FLD. Earlier, Stoughton and Yoon [15] were successfully converted all the experimental ε-FLD of Al 2008 T4 reported by Graf and Hosford [8] into PEPS-FLDs, and formed a narrow band of limiting strains. This confirmed the utility of PEPS-FLD as a path independent measure. Actually the radius in PEPS-FLD represents effective plastic strain which is not directly derived from the principal strain component rather relate with stress tensor matrix with the yield function, as shown in Eq. (7). As it is known that stress state is insensitive to the deformation history; hence, PEPS-FLD is also robust in nature as like as σ-FLD. However, it is observed that the PEPS-FLD has no dependence on the choice of hardening laws. A great advantage of PEPS-FLD over σ-FLD is its shape and appearance. It is seen that PEPS-FLD looks nearly similar to the ε-FLD with a proper distinction of three regions, namely, uniaxial, plane strain, and biaxial. Also, the plane strain limit is the lowest point as similar to the ε-FLD. Hence, the Researchers and Engineers can compare the forming limit and understand the kind of strain path induced during the forming process. On the other hand, it is really difficult for σ-FLD to find its plane strain path until or unless it is specified, and it is also very difficult to compare two different limiting stress diagrams in terms of formability context. Due to these intuitive natures, PEPS-FLD can be readily acceptable to sheet metal forming researchers.

3 Experimental Procedure

3.1 Material Characterization. Two different commercial grade automobile steels of 1.2 mm thickness were considered in the present work: (a) DP steel (DP600) and (b) IF steel. The DP600 steel consists of two phases, i.e., ferrite and martensite structures, as shown in Fig. 4(*a*). This is achieved by intercritical annealing stage during which small particles of austenite phases appear, which under quenching resulted into small volume fraction of martensite islands inside ferrite phases. In IF steel, the interstitial elements like carbon and nitrogen are scavenged by addition of microalloying elements like Ti and Nb. This extreme low-carbon steel has excellent formability due to the absence of interstitial elements like C and N, which adversely affects ductility. The microstructure of IF steel is shown in Fig. 4(*b*).

The stress–strain response of both the steels was evaluated along three directions, viz., 0 deg, 45 deg, and 90 deg with respect

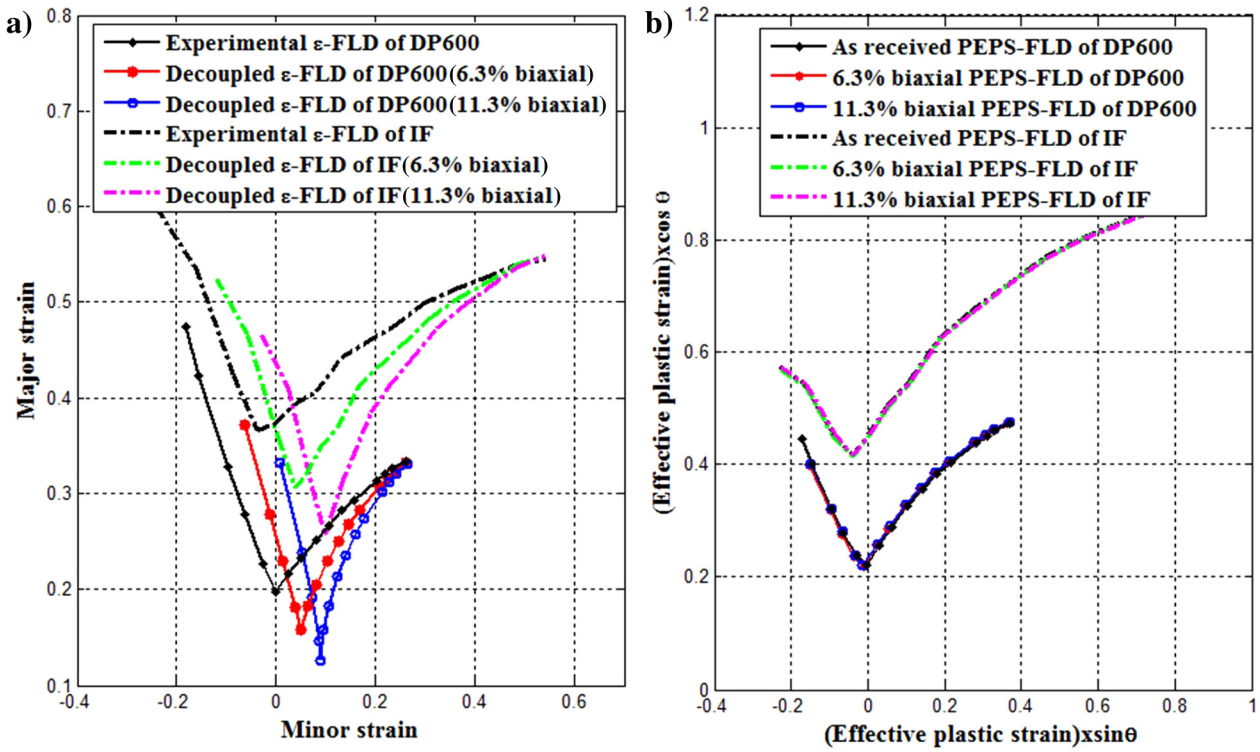

Fig. 3 Predicted (*a*) decoupled theoretical ε-FLD for different prestrain conditions obtained from σ-FLD and (*b*) the convergence of PEPS-FLDs of all decoupled ε-FLDs

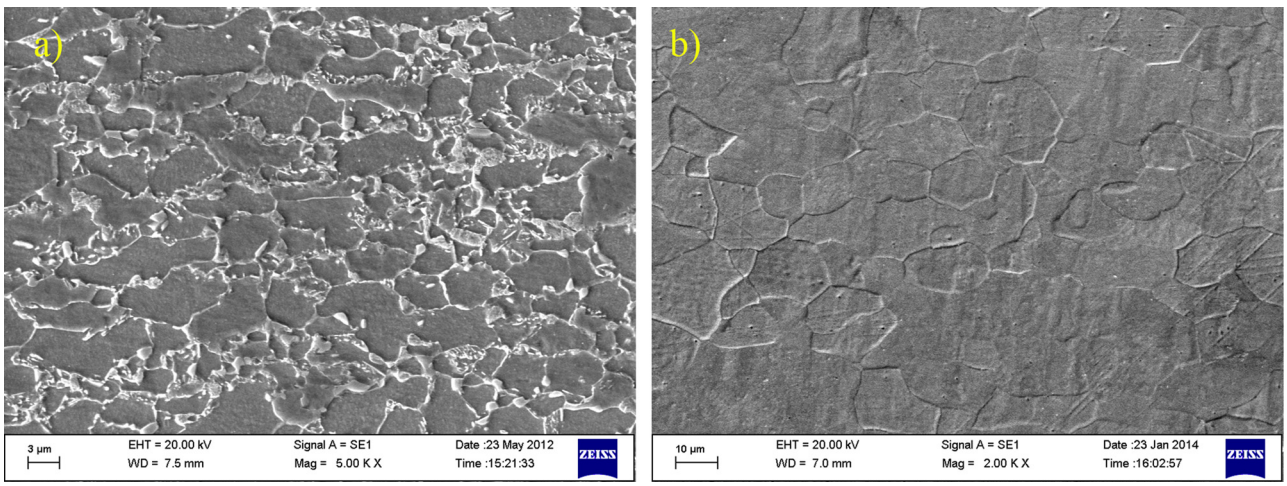

Fig. 4 Microstructure observed in scanning electron microscopy: (*a*) DP600 and (*b*) IF

to rolling direction of the sheet, and the various properties were reported in Table 1. The true stress–true strain data from uniaxial tensile test of DP600 and IF were fitted and extrapolated with the Hollomon, Swift, and modified Voce hardening laws, and the different coefficients were determined by best fitting curves. These different coefficients (as shown in Table 2) were evaluated statistically by best fitting curve with comparing R^2 value in each case.

3.2 Formability Experiments. In this study, complex strain path was developed compounding two linear strain paths. The tensile–tensile prestrain was induced in the sheet metal during the first path or stage, and subsequently, the out-of-plane stretch forming operation was carried out to determine LDH as the measure of formability in the second path or stage.

3.2.1 Prestraining in the First Stage. For this test, an in-plane stretch forming setup, as shown in Fig. 5(*a*), was conceptualized and fabricated as suggested by Raghavan [24]. The sheet metal with brass washer was together placed over the die, and thick film of lubrication was applied between the flat face punch and the washer to avoid the fracture of the washer and/or sheet metal at the corner. The flat punch drove the test specimen indirectly through the washer. Circular grids of 2.5 mm diameter were marked on the blanks by electrochemical etching technique to measure major and minor strains induced in the specimen after deformation. Due to radial friction forces at the sheet–washer

Table 1 Tensile properties of DP600 and IF steels used in the study

Grades and gauges	Yield strength (MPa)	Ultimate tensile strength (MPa)	% total elongation	Anisotropic properties				
				r_0	r_{45}	r_{90}	$\bar{r}$[a]	Δr[b]
DP600 (1.2)	407	665	19.12	0.96	0.93	1.05	0.97	0.08
IF (1.2)	118	272	48.6	1.79	1.54	3.02	1.97	0.87

[a]Normal anisotropy $= \bar{r} = (r_0 + 2r_{45} + r_{90})/4$.
[b]Planar anisotropy $= \Delta r = (r_0 - 2r_{45} + r_{90})/2$.

Table 2 Material constants form different hardening model for both DP600 and IF steels

Material	*Hollomon law*			*Swift law*				*Modified Voce law*				
	K	n	R^2[a]	ε_0	K	n	R^2[a]	A	B_0	B_1	C	R^2[a]
DP600	1125	0.21	0.9836	0.005	1140	0.20	0.9980	839	361	202	10	0.9843
IF	523	0.3	0.9811	0.001	574	0.34	0.9997	408	278	54	06	0.9976

[a]Here R^2 is defined as the *coefficient of determination*, which indicates how well data fit a line or curve.

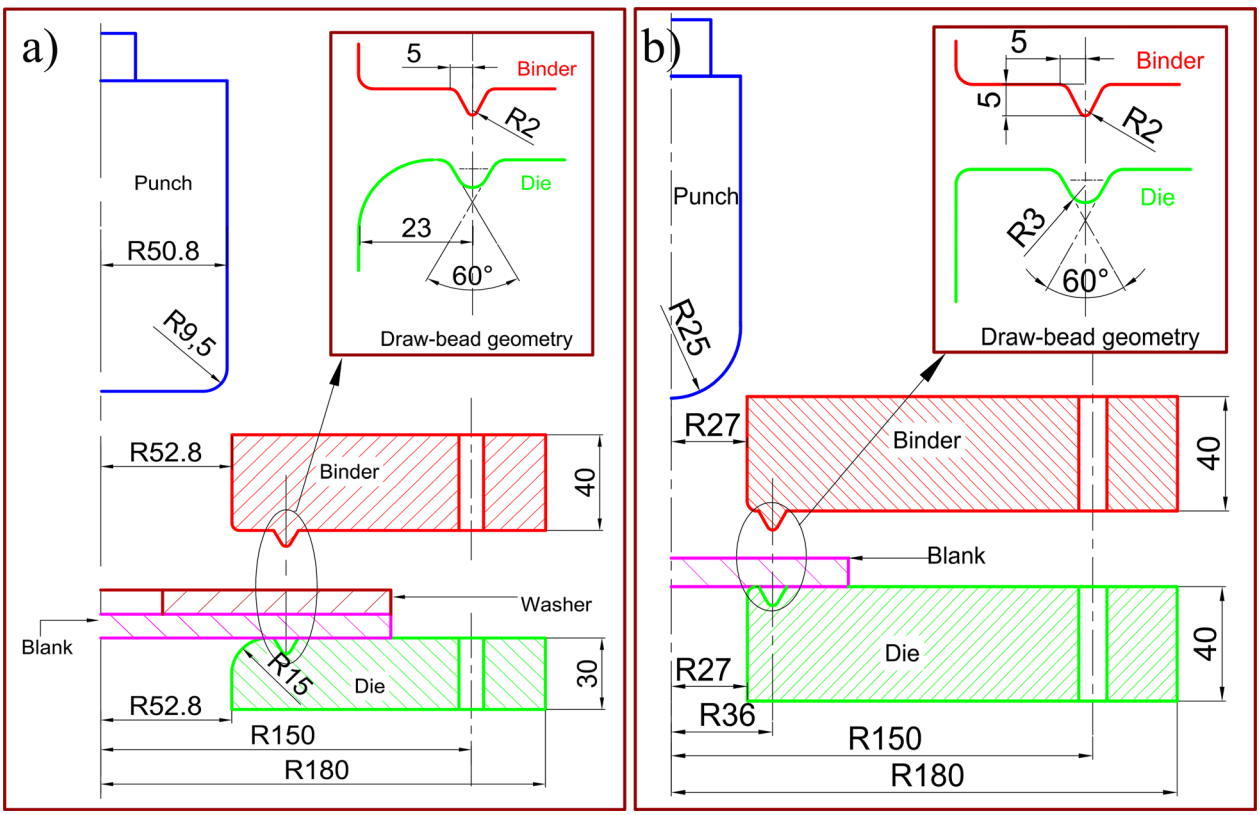

Fig. 5 The schematic of the tooling for the multistage forming operation: (*a*) in-plane prestraining and (*b*) out-of-plane stretch forming for LDH test (all dimensions are in mm)

interface, it was found that nearly equibiaxial prestrain was induced in the specimen. It is important to note that the amount of prestrain induced in the material was predicted by FE simulations, and accordingly, the punch travel was planned in the experiment. Two different levels of prestrain, i.e., 6.3% and 11.3% were planned in the first stage of deformation.

3.2.2 LDH Test of Prestrained Material. After measuring the prestrain induced in the deformed blank, the flat bottom portion was trimmed by wire cut electric discharge machining (WEDM). This trimmed blank was subsequently treated as input test piece for LDH testing. The LDH test was carried out using out-of-plane stretch forming setup by a hemispherical punch, as shown in Fig. 5(*b*). The experiments were stopped when a visible neck or initiation of fracture was observed on the specimens, which was also reflected as the drooping in the load–progression curve.

4 FE Analysis of LDH Test of Prestrained Steel

Mathematical framework of FLD theories coupled with the FE simulation leads to a drastic reduction in the time and cost during the initial adaptation of the tooling design and selection of the

process parameters to get failure-free components. In this work, numerical simulation of both the stages of deformation was carried out using a commercial available FE solver, LS-DYNA-971. The accuracy of the model depends on the selection of the material constitutive properties, boundary conditions, and the damage model. In this work, the deformable blank was modeled using the Barlat-89 nonquadratic yield criterion incorporating both the normal and planar anisotropy properties, as described in Sec. 2.1. The Swift power hardening law was used without incorporating the influence of strain rate sensitive index. The die was fixed, and both the punch and binder were allowed to move in the z direction (along the punch axis). The Coulomb's friction model was assumed between the blank and rigid surfaces using a coefficient of friction of 0.01 in lubricated condition and 0.15 in dry condition. Figure 6 shows the FE model of the double-stage forming sequence, where the prestraining was induced by the in-plane stretch forming process, and the required blank was trimmed to further deform using the out-of-plane stretch forming setup. The experimental ε-FLD and formulated σ-FLD and PEPS-FLD were incorporated in the numerical simulation to evaluate the formability in terms of LDH. In FE analysis, the failure node was identified, and the strain and stress data of this node at different time steps of the deformation were plotted inside the strain and stress domain for both the materials. Figure 7 shows the deformation path during LDH testing of DP600 as-received materials, and it can be observed that the failure is predicted at the same dome height by all the FLDs. However, the σ-FLD incorporating the Swift hardening law predicts the LDH same as ε-FLD and PEPS-FLD.

5 Results and Discussion

5.1 LDH Prediction. The deformed domes after LDH testing of various biaxial tensile prestrained DP600 and IF samples are shown in Fig. 8.

It was observed that the formability index-LDH decreased as the amount of prestrain increased in case of both the materials. The prestrain during the first stage of deformation exhausted some ductility of the material reducing the limiting strains, and hence, the reduction in LDH during the second stage of deformation as compared to a fresh as-received material. It was further observed that the dome height of IF steel was always higher compared to that of DP steel in all prestrain conditions. All the FE predicted LDH results of differently prestrained steels obtained by ε-FLD, σ-FLD, and PEPS-FLD are shown in Fig. 9 in comparison with experimental results. The predicted results by all the three FLDs are equal in the case of as-received material (zero prestrain condition), and these results are comparable with the experimental results within 4% of error. However, the LDH was overpredicted

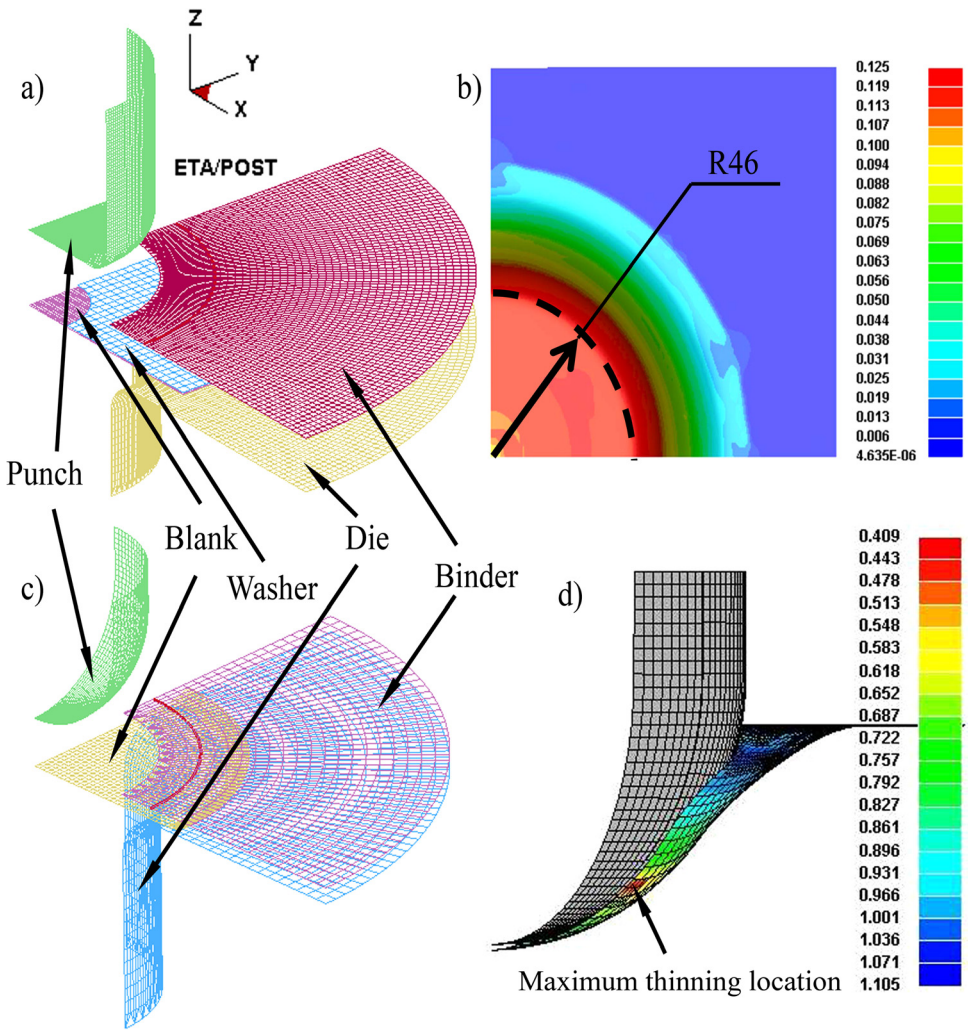

Fig. 6 Numerical process sequences for two-stage forming operation: (*a*) quarter symmetry model of in-plane stretch forming setup, (*b*) deformed specimen after 11.3% prestraining, (*c*) quarter symmetry model of LDH testing of prestrained blank, and (*d*) deformed dome indicating the location of maximum thinning and failure

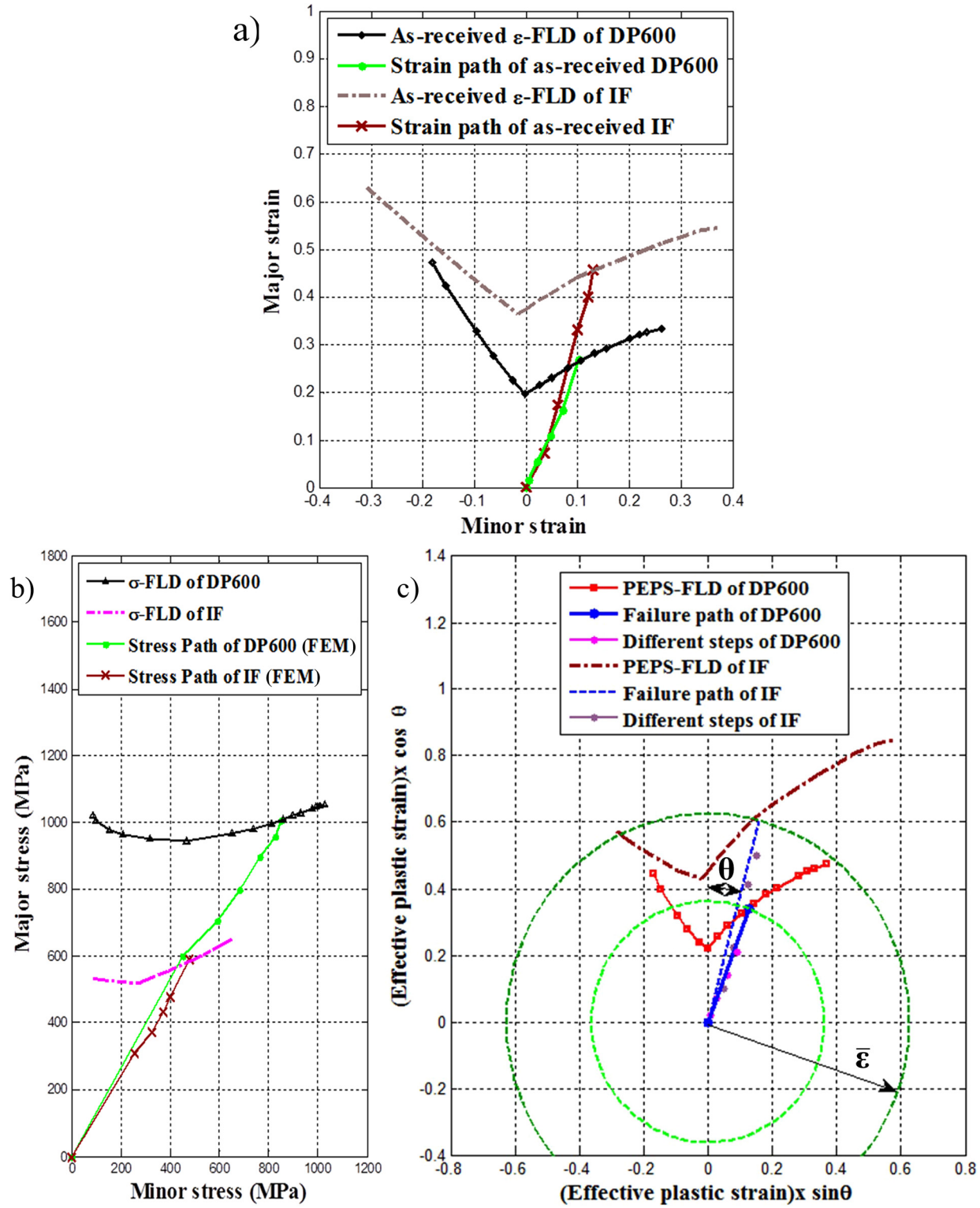

Fig. 7 Deformation path during LDH testing of DP600 as-received material plotted inside (*a*) as-received ε-FLD, (*b*) estimated σ-FLD, and (*c*) PEPS-FLD

by ε-FLD for all the prestrained materials, and on the contrary, the prediction was very close to the experimental results by σ-FLD and PEPS-FLD. The percentage error in the prediction of LDH by different FLDs was computed and compared in Table 3 for both DP600 and IF materials. It can be observed that the prediction error was more in case of prestrained IF steel compared to the DP600 steel. In order to get insight into the formability changes in LDH tests of prestrained materials, the deformation path and the thickness distribution were analyzed in Secs. 5.2 and 5.3.

5.2 Analysis of Deformation Path. The strain and stress paths of the failed region obtained from FE results of both the stages of forming DP600 steel are shown in Fig. 10 with reference

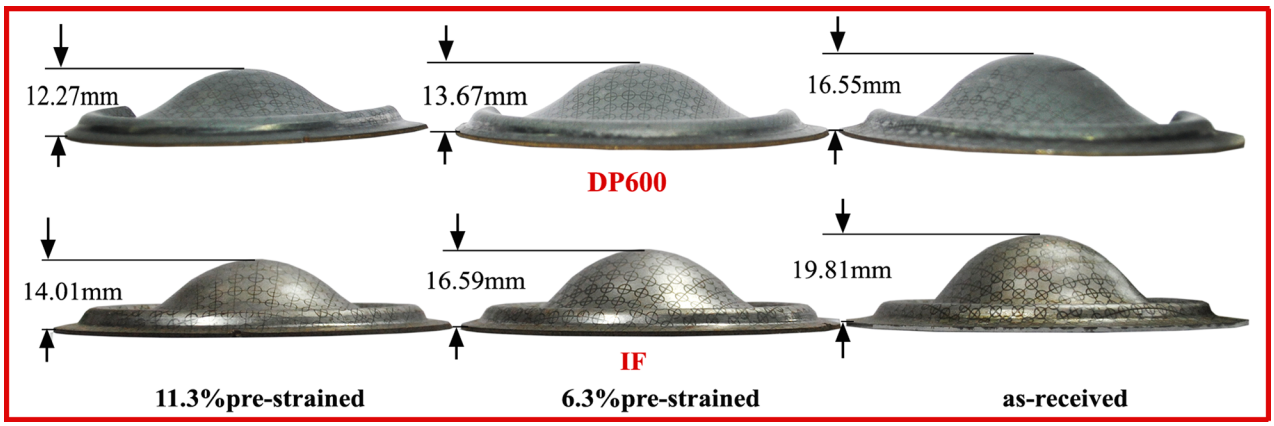

Fig. 8 The deformed cups obtained from LDH testing of different prestrained materials

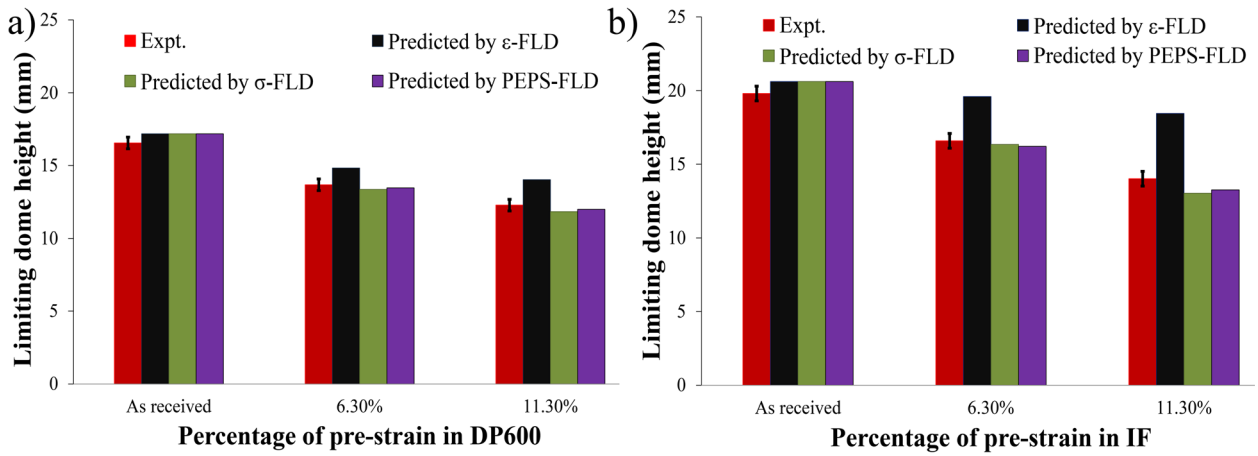

Fig. 9 Comparison of predicted LDH by different FLDs at different prestrained conditions: (*a*) DP600 and (*b*) IF

Table 3 Absolute percentage error in formability prediction of both DP600 and IF steels

		Absolute error in percentage		
Material	% of prestrain	By ε-FLD	By σ-FLD	By PEPS-FLD
DP600	As received	3.82	3.82	3.82
	6.3	8.41	2.34	1.85
	11.3	14.26	3.67	2.36
IF	As received	3.99	3.99	3.99
	6.3	18.14	1.51	1.87
	11.3	31.69	7.01	5.43

to its ε-FLD, σ-FLD, and PEPS-FLD. It can be observed that the strain path during the prestraining in the first stage and the LDH testing in second stage are lying in the right side (with $\rho > 0$) of the ε-FLD. However, the slope of these paths was different due to the selections of different die geometry and process parameters. The measured major and minor strain states obtained after the prestraining matched very well with that of experimental results in all the cases. It can be seen from Fig. 10(*a*) that the strain path touches the ε-FLD at point P corresponding to the LDH of 14.82 mm during the second stage of deformation. However, the corresponding point in the stress domain is P1, which crosses the σ-FLD. Similarly, the deformation path shown in the PEPS domain also crosses the constructed PEPS-FLD with effective plastic strain as the radius. The predicted LDH is closer to the experimental results when the deformation path touches the σ-FLD and the PEPS-FLD at Q1 and Q2. The corresponding point is Q in the strain path, which is lying inside the ε-FLD of the as-received DP600 steel. However, the limiting strain of this biaxial prestrained material decrease through shifting of FLD toward the right side as already shown in Fig. 3(*a*). It is observed that both the σ-FLD and PEPS-FLD are able to predict the formability of prestrained DP600 and IF materials taking care of deformation histories. The limiting strain of IF steel is greater than DP600; hence, for same amount of prestraining the decrease in the limiting strain is more in IF steel as compared to the DP600 steel as can be seen from decoupled theoretical estimated FLDs in Fig. 3(*a*). Hence, the as-received ε-FLD overpredicted the LDH of prestrained IF steel more compared to that in case of DP600 steel.

5.3 Prediction of Thickness Distribution and Load Progression. The deformed cups of DP600 and IF materials were cut along the rolling direction, and the thickness variation was measured at different distances from the reference pole. The thickness distribution with respect to the nondimensional distance ratio (distance from the pole (l)/punch radius (r_p)) as computed from the FE analysis along with experimental data is shown in Fig. 11 for all the prestrain conditions of both the materials. It can be seen from the figure that more nonuniform thickness distribution is taken place in DP600 steel compared to the IF steel, and a maximum thinning/failure is developed at a distance away from the pole corresponding to the location where the cup is out of contact with the punch. As the tools (either punch or dies) were in direct contact with blank, the frictional force between them did not allow thinning to occur at the pole and flange. The uniform thickness distribution of IF steel was attributed due to its higher n-value, as reported in Table 2, and hence, IF steels have higher

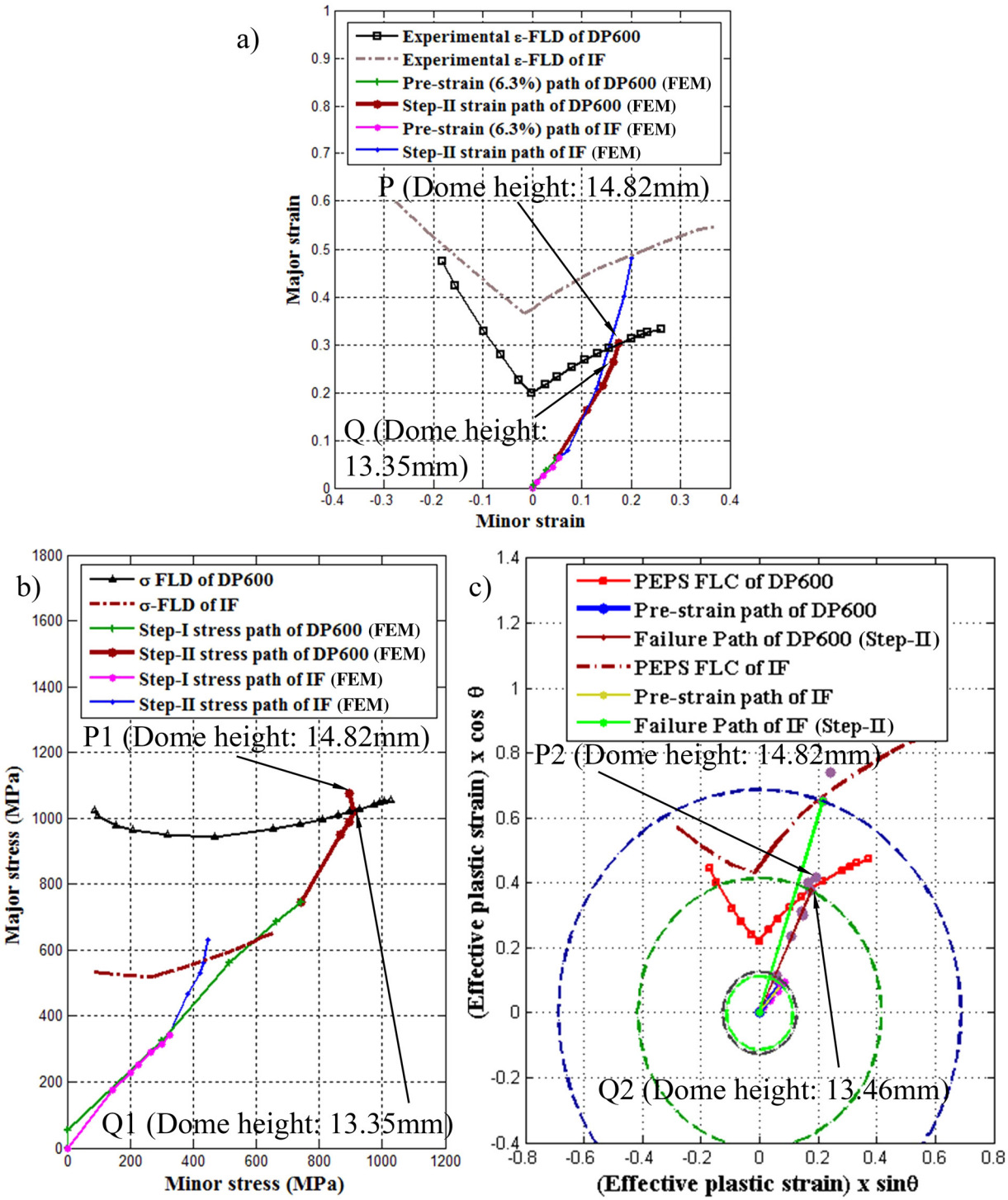

Fig. 10 (*a*) Strain path, (*b*) stress path, and (*c*) PEPS path during forming of 6.3% prestrained DP600 material

LDH compared to DP600 steel in all conditions. The location of the maximum thinning development was measured in the case of all the prestrain deformed cups of both the materials, and the result is shown in Fig. 12. It can be observed that the location of failure depends on the level of prestrain and types of material. The area of contact between the punch and blank increases with the increase in LDH, and hence the location of maximum thinning development.

The gradual load progression during LDH testing was experienced due to the strain hardening of the sheet metal during biaxial stretch forming and the increase in the frictional force at the punch–blank interface. To validate the accuracy of the FE results, the load–progression curves obtained from the FE simulation results were compared with the experimental data captured by data acquisition system, as shown in Fig. 13. The maximum load required to deform the prestrained blank was less compared to the as-received material for both IF and DP600 steel, and this is due to the lower dome height of the prestrained materials. Being a stronger material with higher forming limit stress, the DP600 steel required more load while stretch forming both in prestrained and as-received conditions compared to IF steel. All the thickness distribution and load progression predicted by the FE simulation

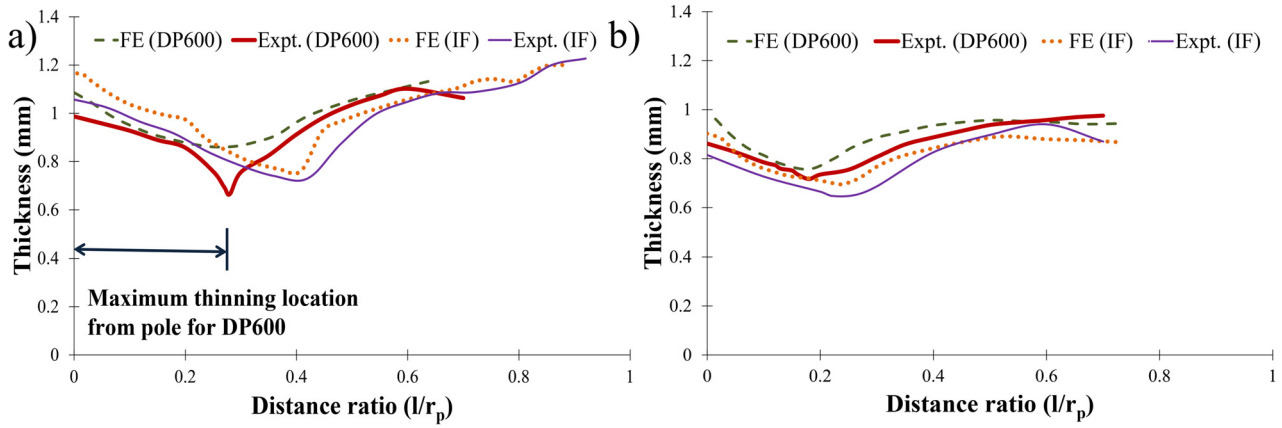

Fig. 11 Comparison of thinning development in DP600 and IF materials in LDH testing: (*a*) as-received material condition and (*b*) 11.3% prestrained condition

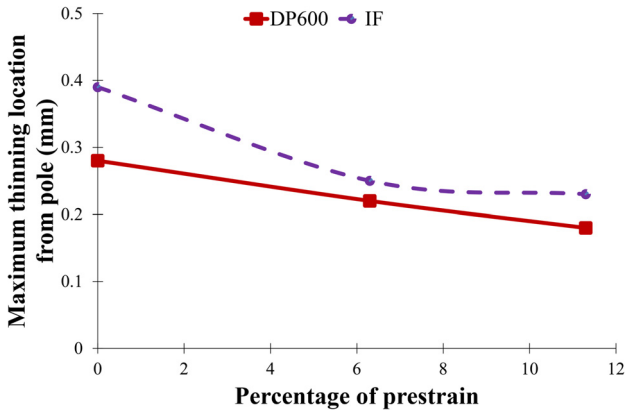

Fig. 12 Variation of maximum thinning location for different prestrained sheet materials

were in good agreement with the experimental results, which validated a successful model incorporating the σ-FLD and PEPS-FLD.

6 Conclusions

The formability was evaluated successfully using the laboratory scale multistage forming processes for both DP600 and IF steels. The FE analysis was done incorporating the theoretical estimated σ-FLD and PEPS-FLD to predict the forming behavior. The current experimental and numerical investigation led to the following major conclusions:

(1) The σ-FLD and PEPS-FLD were estimated successfully for both the IF and DP600 steels using the Barlat-89 anisotropy material model, and it was found that the σ-FLD was significantly depended on the selection of the hardening model.
(2) The PEPS-FLD is insensitive to deformation history with no dependence on the choice of hardening laws. It was

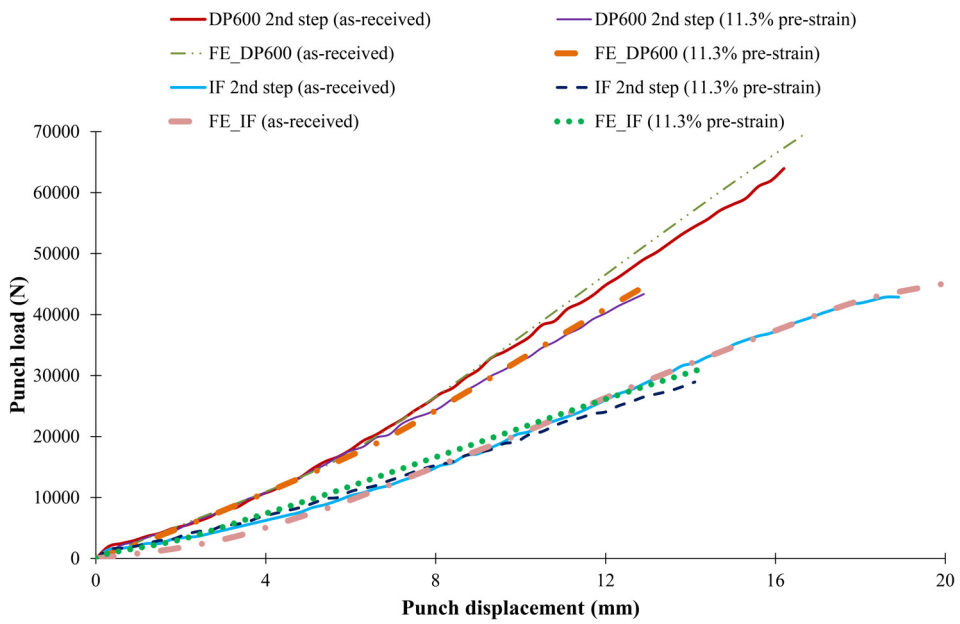

Fig. 13 Validation of FE predicted load-progression curve for as-received and prestrained materials

found that the σ-FLD incorporating the Swift hardening law predicted the LDH same as ε-FLD and PEPS-FLD for as-received DP600 and IF steel sheets.

(3) It was observed that the formability index-LDH decreased as the amount of prestrain increased in case of both the materials. However, the LDH was overpredicted by ε-FLD for all the prestrained materials, and on the contrary, the prediction was very close to the experimental results by σ-FLD and PEPS-FLD.

(4) The decrease in the limiting strain with prestraining is more in IF steel as compared to the DP600 steel. Hence, the as-received ε-FLD overpredicted the LDH of prestrained IF steel more compared to that in case of DP600 steel.

(5) It was observed that the location of maximum thinning development and subsequent failure in the LDH testing depended on the level of prestrain and types of material. The thinning development and load progression during the LDH testing of prestrained materials were predicted successfully by the FE model using both the σ-FLD and PEPS-FLD.

Acknowledgment

The authors are greatly thankful to Dr. Rahul Verma of TATA steel, Jamshedpur, India for providing the sheet metals used in the present study.

Nomenclature

$a, c, h,$ and p = coefficients of Barlat-89 yield criterion related to material anisotropy
$A, B_0, B_1, \varepsilon_0$ = material constants
K = strength coefficient
k_1, k_2 = stress tensor invariants
M = Barlat yield exponent
n = strain hardening exponent
r = Lankford's anisotropy parameter
α = stress ratio
ε = true strain
$\bar{\varepsilon}$ = effective strain
ε_1 = major strain
ε_2 = minor strain
ξ = ratio of effective stress to major stress
ρ = strain ratio
$\bar{\sigma}$ = effective stress
σ_1 = major stress
σ_2 = minor stress

References

[1] Keeler, S. P., and Backofen, W. A., 1963, "Plastic Instability and Fracture in Sheets Stretched Over Rigid Punches," ASM Trans. Q., **56**(1), pp. 25–48.
[2] Goodwin, G. M., 1968, "Application of Strain Analysis to Sheet Metal Forming Problems in the Press Shop," SAE Technical Paper No. 680093.
[3] Banabic, D., and Pöhlandt, K., eds., 2000, *Formability of Metallic Materials: Plastic Anisotropy, Formability Testing, Forming Limits*, Springer Science & Business Media, Berlin.
[4] Hu, J., Marciniak, Z., and Duncan, J., eds., 2002, *Mechanics of Sheet Metal Forming*, Butterworth-Heinemann, Oxford, UK.
[5] Matsuoka, T., and Sudo, C., 1969, "Effect of Strain Path on the Fracture Strain of Steel Sheet," Sumitomo Search, **1**, pp. 71–80.
[6] Muschenborn, W., and Sonne, H. M., 1975, "Effect of Strain Path on the Forming Limits of Sheet Metal," Arch. Eisenhuttenwes., **46**(9), pp. 597–602.
[7] Laukonis, J. V., and Ghosh, A. K., 1978, "Effects of Strain Path Changes on the Formability of Sheet Metals," Metall. Trans. A, **9**(12), pp. 1849–1856.
[8] Graf, A. F., and Hosford, W. F., 1993, "Calculations of Forming Limit," Metall. Trans. A, **24**(11), pp. 2497–2501.
[9] Kleemola, H. J., and Pelkkikangas, M. T., 1977, "Effect of Predeformation and Strain Path on the Forming Limits of Steel, Copper and Brass," Sheet Met. Ind., **64**(6), pp. 591–592.
[10] Arrieux, R., Bedrin, C., and Boivin, M., 1982, "Determination of an Intrinsic Forming Limit Stress Diagram for Isotropic Sheets," 12th Biennial Congress of the International Deep Drawing Research Group, Santa Margherita Ligure, Italy, May 24–28, Associazione Italiana di Metallurgia, Milan, Italy, Vol. 2, pp. 61–71.
[11] Stoughton, T. B., 2000, "A General Forming Limit Criterion for Sheet Metal Forming," Int. J. Mech. Sci., **42**(1), pp. 1–27.
[12] Stoughton, T. B., 2001, "Stress-Based Forming Limits in Sheet-Metal Forming," ASME J. Eng. Mater. Technol., **123**(4), pp. 417–422.
[13] Yoshida, K., Kuwabara, T., and Kuroda, M., 2007, "Path-Dependence of the Forming Limit Stresses in a Sheet Metal," Int. J. Plast., **23**(3), pp. 361–384.
[14] Zeng, D., Chappuis, L., Xia, Z. C., and Zhu, X., 2008, "A Path Independent Forming Limit Criterion for Sheet Metal Forming Simulations," SAE Technical Paper No. 2008-01-1445.
[15] Stoughton, T. B., and Yoon, J. W., 2012, "Path Independent Forming Limits in Strain and Stress Spaces," Int. J. Solids Struct., **49**(25), pp. 3616–3625.
[16] Olsen, T. Y., 1920, "Machines for Ductility Testing," Proc. Am. Soc. Mater., **20**, pp. 398–403.
[17] Hecker, S. S., 1975, "Formability of Aluminum Alloy Sheets," ASME J. Eng. Mater. Technol., **97**(1), pp. 66–73.
[18] Marciniak, Z., and Kuczyński, K., 1967, "Limit Strains in the Processes of Stretch-Forming Sheet Metal," Int. J. Mech. Sci., **9**(9), pp. 609–620.
[19] Nakazima, K., Kikuma, T., and Hasuka, K., 1968, "Study on the Formability of Steel Sheets," Yawata Technical Report No. 264.
[20] Hasek, V., 1973, "On the Strain and Stress States in Drawing of Large Un-Regular Sheet Metal Components," Berichte aus dem Institut für Umformtechnik, Universität Stuttgart, Essen, Germany, Report No. 25 (in German).
[21] Barlat, F., and Lian, K., 1989, "Plastic Behavior and Stretchability of Sheet Metals. Part I: A Yield Function for Orthotropic Sheets Under Plane Stress Conditions," Int. J. Plast., **5**(1), pp. 51–66.
[22] Kilfoil, L. J., 2007, "In-Plane Plane Strain Testing to Evaluate Formability of Sheet Steels Used in Tubular Products," M.S. thesis, Queen's University, Kingston, ON, Canada.
[23] Panda, S. K., 2007, "Formability of Tailor Welded Blanks of Low Carbon Steel in Stretch Forming," Doctoral thesis, Indian Institute of Technology, Delhi, India.
[24] Raghavan, K. S., 1995, "A Simple Technique to Generate In-Plane Forming Limit Curves and Selected Applications," Metall. Mater. Trans. A, **26**(8), pp. 2075–2084.